Article

Structures and Role of the Intermediate Phases on the Crystallization of BaTiO₃ from an Aqueous Synthesis Route

Kristine Bakken, Viviann H. Pedersen, Anders B. Blichfeld, Inger-Emma Nylund, Satoshi Tominaka, Koji Ohara, Tor Grande, and Mari-Ann Einarsrud*
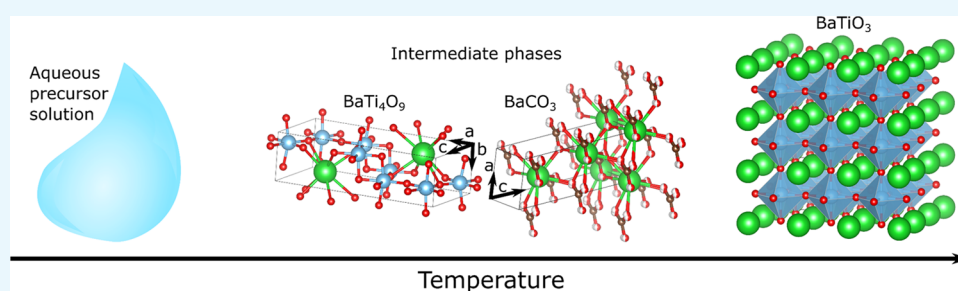
Read Online

ACCESS | Metrics & More | Article Recommendations | Supporting Information

ABSTRACT: Carbonate formation is a prevailing challenge in synthesis of BaTiO₃, especially through wet chemical synthesis routes. In this work, we report the phase evolution during thermal annealing of an aqueous BaTiO₃ precursor solution, with a particular focus on the structures and role of intermediate phases forming prior to BaTiO₃ nucleation. *In situ* infrared spectroscopy, *in situ* X-ray total scattering, and transmission electron microscopy were used to reveal the decomposition, pyrolysis, and crystallization reactions occurring during thermal processing. Our results show that the intermediate phases consist of nanosized calcite-like BaCO₃ and BaTi₄O₉ phases and that the intimate mixing of these along with their metastability ensures complete decomposition to form BaTiO₃ above 600 °C. We demonstrate that the stability of the intermediate phases is dependent on the processing atmosphere, where especially enhanced CO₂ levels is detrimental for the formation of phase pure BaTiO₃.

1. INTRODUCTION

The thermodynamic stability of BaCO₃ poses a common synthesis challenge for producing BaTiO₃, which is a ferroelectric material widely used in capacitors.[1] The stability of BaCO₃ relative to BaTiO₃ increases with a high partial pressure of CO₂ in the atmosphere and analogously with the activity (concentration) of CO₂ in water.[2] Moreover, the solubility of BaCO₃ in water is limited,[3] which combined with the thermodynamic stability makes carbonate secondary phases prevalent both in solid-state reactions and aqueous processing of BaTiO₃ materials. The affinity for carbonate formation arises from the basicity of BaO combined with the abundance of CO₂ in the atmosphere but also dissolved in water. Similar synthesis challenges are observed in other Ba-containing oxides or ceramics consisting of basic oxides.[4]

Wet chemical synthesis studies of BaTiO₃-based powders and thin films generally report BaCO₃ compounds as intermediate and secondary phases.[1,5] Using sol−gel-related methods based on organic solvents, the precursors tend to decompose to form aragonite-type carbonate (BaCO₃ (A)) and TiO₂, where BaTiO₃ nucleates through the solid-state reactions of these above 600 °C.[6−10] However, in Pechini-based synthesis methods and from aqueous processing, a so-called oxycarbonate phase with the global proposed stoichiometry Ba₂Ti₂O₅CO₃ is observed.[10−20] Recently, aqueous chemical solution deposition (CSD) synthesis routes for BaTiO₃-based thin films have been reported,[21−23] where this intermediate oxycarbonate phase was observed to form prior to the perovskite, dependent on the thermal processing. The pyrolysis reactions and the formation of the oxycarbonate were reported to play an integral part in the texture formation, phase purity, and quality of the films.[22,23] The oxycarbonate seems to inhibit the formation of BaCO₃ (A) and therefore also shifts the BaTiO₃ formation from the solid-state reaction of TiO₂ and BaCO₃ (A) to proceed through decomposition of the oxycarbonate. The formation of the intermediate oxy-carbonate phase has been linked to the presence of a "carbonate-like" linkage in the barium carboxylates[24] or to the formation of a mixed metal citric acid complex in the precursor solution.[12−17]

Table 1. Comparison of the Structures of the Aragonite- and Calcite-Type BaCO₃[a]

	aragonite BaCO₃	calcite BaCO₃
crystal structure	$Pmcn$ (nr. 62)	$R\bar{3}mH$ (nr. 160)
IR-active absorption bands [cm⁻¹]	697, 856, 1059, 1435	693, 875, 1059, 1390−1435
bond lengths [Å]		
Ba−Ba	4.35, 4.357, 4.528	4.615
B−C	3.19, 3.247, 3.63, 3.734	3.35, 3.637, 4.954
Ba−O	2.705, 2.708, 2.783, 2.824, 2.86, 4.394, 4.398, 4.467, 4.486, 4.513, 4.556, 4.611, 4.647, 4.858	2.706, 3.004, 4.296, 4.49

[a]Based on refs 19, 20, 34, 36, 38

Several local structures for the oxycarbonate phase have been proposed based on the overall global structure of $Ba_2Ti_2O_5CO_3$.[15−18] However, Ischenko et al. observed that the intermediate oxycarbonate locally consisted of Ba- and Ti-rich nanosized regions, where there was no clear single crystalline structure in the Ti-rich area but instead a range of Ba_yTiO_{2+y} phases were observed.[19] The Ba-rich areas had a structure close to the high-temperature calcite-type polymorph of $BaCO_3$ ($R\bar{3}mH$, no. 166),[19,20] where substitution of CO_3^{2-} with O^{2-} stabilized the calcite structure giving $BaO_x(CO_3)_{1-x}$.[19,20] The proposed general reaction for the transformation pathway of $BaTiO_3$ was through the formation of this intermediate oxycarbonate phase:

$$(Ba, Ti)\text{-precursor complex}$$
$$\rightarrow Ba_yTiO_{2+y} + BaO_x(CO_3)_{1-x}$$
$$\rightarrow BaTiO_3 + CO_2 \tag{1}$$
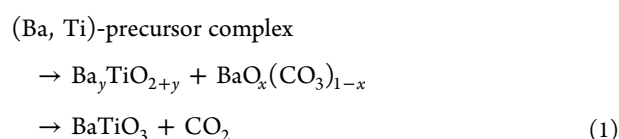
The $BaO_x(CO_3)_{1-x}$ phase was observed to form preferably in the presence of titanium.[19,20] Hence, a second stabilizing mechanism was also proposed by Ischenko et al.: topotaxial formation of structural domains of calcite-type carbonate ($BaCO_3$ (C)) by templating with oxygen-deficient Ti-rich $BaTiO_3$-like structures.[20] A comparison of the aragonite and calcite modifications of $BaCO_3$ can be found in Table 1. Although the models for the intermediate phases have been proposed, it is not known how these phases are affected by processing conditions, such as the heating rate, annealing temperature, and atmosphere, and the intermediate phases influence the formation of $BaTiO_3$.

In situ characterization is a rapidly growing field as studying materials under real-time conditions is necessary for further development, especially in battery research[25,26] and hydrogen technology.[27] Moreover, as new synthesis methods are implemented for complex material systems, much insight into the reaction pathway is required, where in situ techniques are becoming more prominent.[28−31] *In situ* studies by X-ray diffraction on $BaTiO_3$ are reported both during deposition[32,33] and the annealing[22] of thin films.

Here, we report the thermal decomposition and phase evolution for $BaTiO_3$ powders from an oxycarbonate forming aqueous synthesis route. *In situ* infrared (IR) spectroscopy and synchrotron X-ray total scattering were used to study the decomposition of the precursor, formation of intermediate phases, and nucleation of $BaTiO_3$ from the intermediate phases. Moreover, the effect of partial pressure of CO_2 during the decomposition was investigated. Rietveld and pair distribution function (PDF) refinements revealed the global and local structures of the intermediate phases present in the powders before $BaTiO_3$ nucleation, supported by electron microscopy. The intermediate phases were found to consist of

$BaCO_3$ (C) and a $BaTi_4O_9$ phase; however, the formation of these depends heavily on the processing conditions, especially the heating rate, and partial pressure of CO_2.

2. RESULTS

2.1. *In Situ* Characterization during Thermal Annealing of BaTiO₃ Precursor Powders. Figure 1 shows the in
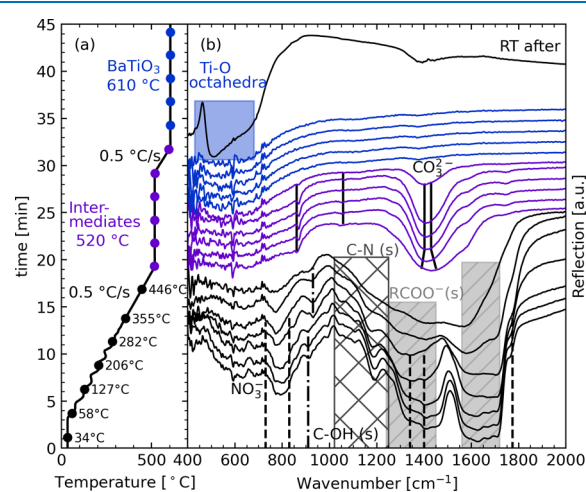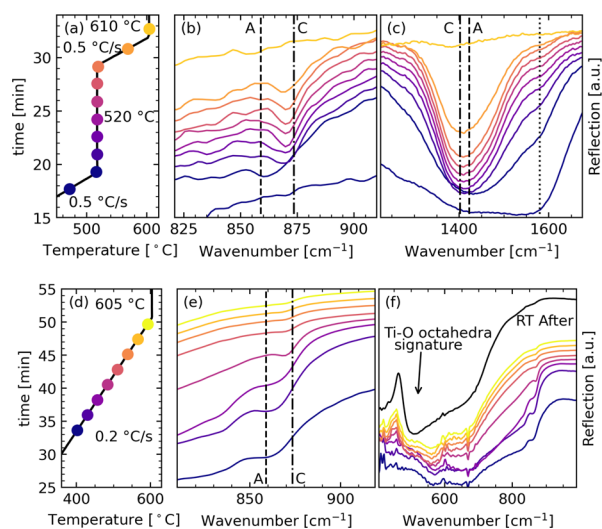

Figure 1. (a) Temperature profile and (b) in situ IR spectra of a $BaTiO_3$ precursor powder showing the phase evolution during annealing in synthetic air to 610 °C with a hold step at 520 °C. Bands assigned to the functional groups in the precursor are indicated along with the $BaCO_3$ bands developing at higher temperatures, and the signature of the Ti−O octahedra band is indicated for the spectrum recorded at room temperature (RT after).

situ IR spectra of the $BaTiO_3$ precursor powder during annealing in synthetic air with a hold step at 520 °C to facilitate formation of the intermediate phases. (The full spectra are included in Figure S2.) The IR spectrum of the amorphous as-prepared precursor contained a split asymmetric stretching (as) mode (1340 and 1400 cm⁻¹) of NO_3^-, showing a perturbation of the nitrate ion by cation interactions.[34,35] The symmetric stretching (ss, 1240−1450 cm⁻¹) and as- (1590−1750 cm⁻¹) modes for the carboxylic acid groups originating from EDTA, citric acid, and their derivatives are indicated as wide bands, reflecting bonding to different metal ions.[34,35] The frequency range for the as-band of the nitrate and carboxylic acid groups overlap, so the intensity of the wide band also has a contribution from the nitrate. The characteristic C−OH out-of-plane (oop) bending mode for carboxylic acid groups was observed at 930 cm⁻¹. The C−N stretching mode (1020−1250 cm⁻¹) from the EDTA derivatives was identified as a wide band.[34,35] As the temperature is increased above 200 °C, the intensity of the bands decreases due to the decomposition

of the nitrate. Between 300 and 400 °C, the bands assigned to the different functional groups in the precursor merge to a wide band (1000−1800 cm^{-1}). In the temperature range of 470−520 °C, this wide band narrows to the asymmetric stretching band of the carbonate ion. Carbonate species remain in the powder until 610 °C where there is only BaTiO$_3$, as seen from the absence of other bands in the *in situ* spectra and from the *ex situ* spectrum taken from the same sample after cooling (marked "RT after"). These observations correspond well with the IR spectra reported for calcined powders from the same precursor solution, where the carbonate absorption band was observed in the temperature range of 450−650 °C.[21]

The IR spectra from Figure 1 in the temperature region where carbonate species are present are shown in greater detail in Figure 2a−c. A shift in the carbonate frequencies was


Figure 2. *In situ* IR spectra of BaTiO$_3$ precursors annealed with different temperature programs. (a) Temperature profile and IR spectra in the frequency range of (b) the out-of-plane vibrational mode and (c) the asymmetric stretching mode of BaCO$_3$, measured in synthetic air. (d) Temperature profile and IR spectra in (e) the frequency range for the out-of-plane vibrational mode of BaCO$_3$ and (f) the low frequency range, measured in an ambient atmosphere and without instrument vacuum. The absorption bands of BaCO$_3$ (A) are indicated as A and of BaCO$_3$ (C) as C.

observed for both the oop and as-bands with increasing temperature from those of BaCO$_3$ (A) (861 and 1430 cm^{-1}) to those of BaCO$_3$ (C) (871 and 1402 cm^{-1}),[34] which is a commonly reported feature of the intermediate oxycarbonate phase.[15−20] Broad bands developed at the start of the hold period became sharper with prolonged annealing, and the frequencies shifted toward that of calcite. Isothermal formation of the intermediate phases and heating with a low heating rate (Figure S3) were also investigated and showed the same trends for the carbonate band development. The wide carbonate as-band was also accompanied by shoulders at 1580 and at 1280 cm^{-1} in some cases (summarized in Table S1). It is proposed that the shoulders could be assigned to a splitting of the asymmetric stretching band of CO$_3^{2-}$ bonded to Ti^{4+} as the presence of titanium is necessary for the BaCO$_3$ (C) formation (Figure S4).

To ease the comparison of the development of the bands assigned to the perovskite and the carbonate, a BaTiO$_3$ precursor powder was heated without the dome of the

reaction chamber and no instrument vacuum. The *in situ* IR spectra of the precursor in the temperature region of the formation of intermediates and decomposition are shown in Figure 2d−f. The carbonate oop-band (Figure 2e) and as-band (not shown) were visible above 400 °C, similar to the sample with a hold step (Figure 2b). The oop-band was seen as a wide feature at the aragonite frequency (859 cm^{-1}) but shifted toward that of calcite (871 cm^{-1}) as the temperature increased. No shoulder accompanying the as-band was observed for this heating program. The signature of the perovskite band associated with the Ti−O octahedra (Figure 2f) was observed at 500 °C and became more pronounced as the temperature increased. The formation of the perovskite band (Figure 2f) was accompanied with the formation of BaCO$_3$ (C) (Figure 2e), and as the perovskite band became more pronounced, the carbonate oop-band decreased in intensity, showing how the BaCO$_3$ (C) decomposes and BaTiO$_3$ is formed.

The total scattering patterns and converted PDFs of the BaTiO$_3$ precursor powder heated *in situ* with a heating rate of 0.17 °C/s are shown in Figure 3 (and Figure S5). The
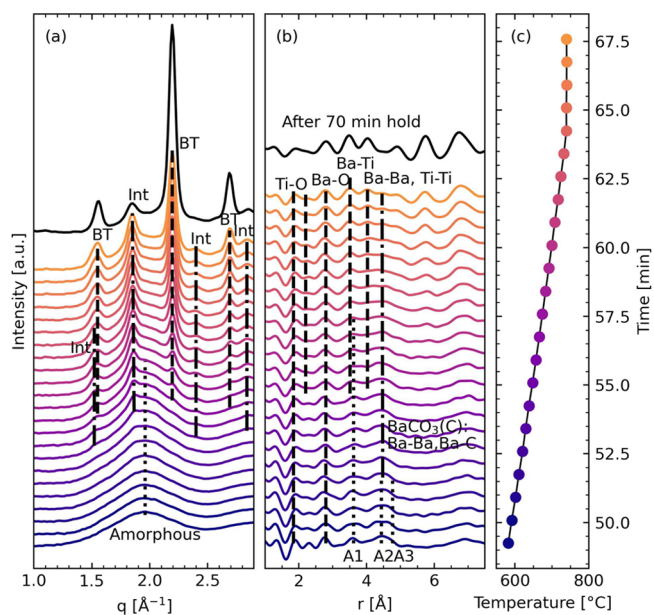

Figure 3. (a) Measured total scattering, (b) the converted PDFs, and (c) temperature profile for a BaTiO$_3$ precursor powder heated with a heating rate of 0.17 °C/s to 734 °C in synthetic air. The diffraction lines in panel (a) are indicated as "BT" for BaTiO$_3$ and "Int" for the intermediate BaCO$_3$ (C) and BaTi$_4$O$_9$ phases. A broad feature corresponding to amorphous aragonite-like carbonate is also indicated. The atomic pair distances are indicated in panel (b) for the BaTiO$_3$ phase, BaCO$_3$ (C), and an amorphous phase. In the amorphous phase, several overlapping atomic pair distances exist for each of the indicated peaks. Peak A1 corresponds to a Ba−C distance in BaCO$_3$ (A) and Ba−Ba, Ba−Ti, and Ti−O distances in a BaTi$_4$O$_9$ phase. Peak A2 corresponds to Ba−Ba and Ba−O distances in BaCO$_3$ (A). The A3 peak corresponds to a Ba−O distance in BaCO$_3$ (A) and a Ba−Ti distance in the BaTi$_4$O$_9$ phase.

diffraction patterns (Figure 3a) demonstrate that the sample is amorphous until diffraction lines corresponding to intermediate phases appear at 630 °C, quickly followed by BaTiO$_3$ crystallization at 690 °C. The crystallinity of the BaTiO$_3$ phase is poor but increases during a hold period of 70 min at 734 °C. The PDF (Figure 3b) further demonstrates that the sample is amorphous at low temperatures but transforms into the

intermediate phases with increasing temperature and that no long-range order is observed until crystallization of $BaTiO_3$ occurs. The shortest Ti–O and Ba–O bonds (marked in Figure 3) remain unchanged even going from the amorphous phases at low and intermediate temperatures and through crystallization of $BaTiO_3$. Three additional peaks were identified in the PDFs of the amorphous powder, and a certain local structural change is seen upon formation of the intermediate phases. No long-range structure is observed, indicating that the intermediate phases are nanocrystalline. $BaTiO_3$ crystallization was accompanied by the emergence of peaks in the PDFs from the periodic Ba–Ti, Ba–Ba, and Ti–Ti distances and progressively enhanced long-range order.

2.2. Structural Investigation of the Intermediate Phases.
Selected converted and refined PDFs are shown in Figure 4 for $BaTiO_3$ precursor powders during different stages
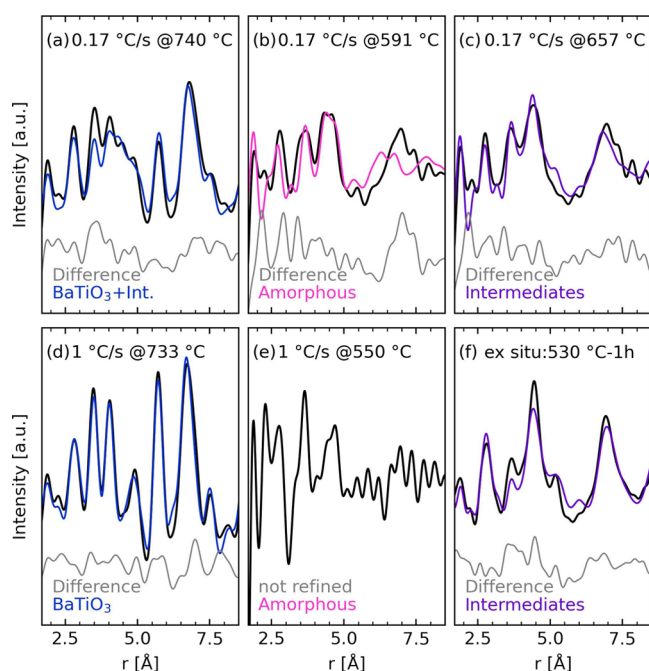

Figure 4. Converted and refined PDFs for $BaTiO_3$ precursor powder with different annealing conditions. (a–c) BaTiO3 precursor powder measured during *in situ* heating with a 0.17 °C/s heating rate in air. (d,e) $BaTiO_3$ precursor powder measured during *in situ* heating with a 1 °C/s heating rate in air. (f) $BaTiO_3$ precursor powder annealed *ex situ* at 530 °C for 1 h in air, total scattering data recorded at ambient temperature. Intermediate phases are marked "Int" or "intermediates".

of the thermal annealing. The refinement of crystalline $BaTiO_3$ (Figure 4a,d) shows a reasonable fit using a rhombohedral

local structure for $BaTiO_3$ ($R3m$, nr. 160[36−38]), although there are deviations indicating a form of local disorder that could not be refined with periodic structures. The refined PDF for the crystallized powder heated with 0.17 °C/s (Figure 4a) also has a contribution from the intermediate phases. The refined PDF for the amorphous powder (prior to any crystallization) is shown in Figure 4b (0.17 °C/s), where the nearest atomic pair distances found in the $BaCO_3$ (A) and $BaTi_4O_9$ structures correspond well with the experimental data, but these phases do not give the correct long-range structure. Using 1 °C/s, the PDFs of the amorphous powder (Figure 4e, the full temperature range is shown in Figures S6 and S7) show sharp and narrow peaks. Both amorphous powders (Figure 4b,e) have peaks that can be described by short-range distances found in $BaCO_3$ (A) and $BaTi_4O_9$. The intermediate phases only formed using 0.17 °C/s (Figure 4c), which had a contribution to the PDF from the amorphous phase compared to the *ex situ* annealed powder (Figure 4f), impacting the scale factor and crystallite sizes. However, both PDFs were fitted with a $BaCO_3$ (C) structure ($R3m$, nr. 160[38,39]) and a $BaTi_4O_9$ phase ($Pmmn$, nr. 59[37]), and the ratio between these was locked to 75:25 during refinements, keeping with the global stoichiometry. The CO_3^{2-} in the calcite structure was allowed full rotational freedom. However, the carbonate groups were observed to only exhibit slight vibrations around their equilibrium position, which eliminate the mirror plane compared to the calcite structure reported by Ischenko *et al.*[19,20] There is an uncertainty associated with the refined structure and composition of the $BaTi_4O_9$ phase as the PDF pattern of the intermediates is largely dominated by the signal from the carbonate (Figure S8). Furthermore, the obtained fit of the intermediate phases indicates that a periodic structure cannot fully represent the local structure; hence, local disorder is expected. Refined lattice parameters for the PDFs displayed in Figure 4 are listed in Table S2.

The intermediate phases were also investigated by TEM imaging of a $BaTiO_3$ precursor powder that was preannealed at 530 °C for 1 h. The TEM bright-field (BF) images and selected area diffraction patterns (SADPs) of selected particles are shown in Figure 5, demonstrating that the crystallinity of the intermediate phases was limited. However, both nanocrystalline and poorly crystalline $BaTiO_3$ particles (Figure 5a,b, respectively) were observed in the powder even if the XRD patterns[21] do not show $BaTiO_3$ at this temperature (530 °C). Separate $BaCO_3$ (C) (Figure 5c) and $BaTi_4O_9$ (Figure 5d,e) crystallites were also identified based on the SADP, although the crystallinity of these particles was also low. The diffraction from the presence of $BaTi_4O_9$ in Figure 5d also includes a contribution from $BaCO_3$ (A) and possibly also $BaCO_3$ (C). The particle in Figure 5f showed diffraction both from the
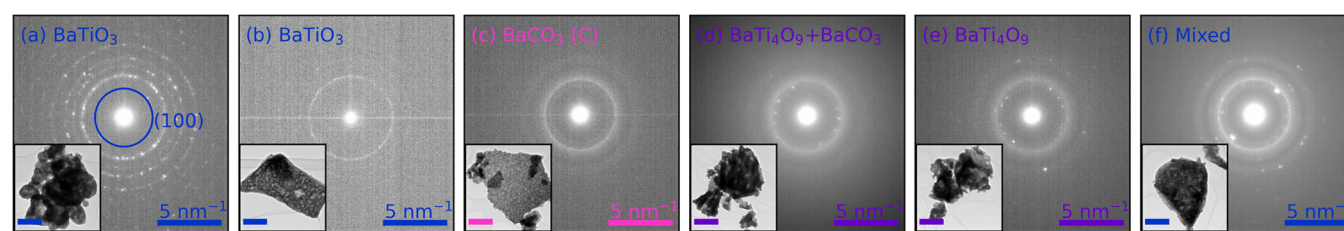
Figure 5. TEM SADP from the center of different particles in a $BaTiO_3$ precursor powder annealed at 530 °C for 1 h in air. The insets show BF images of the particles, where the scale bars correspond to 200 nm. The imaged particles were identified as (a) $BaTiO_3$, (b) $BaTiO_3$, (c) $BaCO_3$ (C), (d) $BaTi_4O_9$ and $BaCO_3$ (A), (e) $BaTi_4O_9$, and (f) mixture of different phases.

$BaCO_3$ (C) and $BaTi_4O_9$ phases. A large crystallite of the $BaTi_4O_9$ phase was probed, giving strongly directional diffraction (2 strong spots) with a d-spacing of 3.638 Å. This d-spacing, corresponding to the (110) planes, is slightly larger in the mixed particle (Figure 5f) than the diffraction spots seen in the $BaTi_4O_9$ particle (Figure 5e), illustrating the change in unit cell with increasing crystallinity. A weak diffraction ring with a d-spacing of 4.065 Å is observed in the particle in Figure 5f, which could correspond to the (101) diffraction line of $BaCO_3$ (C), but it could also be the emerging (100) diffraction of $BaTiO_3$. The identified d-spacings of the particles in Figure 5 are summarized in Table S3.

2.3. Variable CO_2 Partial Pressure during Annealing of $BaTiO_3$ Precursors. Since CO_2 is released during the decomposition and formation of $BaTiO_3$ according to the proposed reaction in eq 1, the partial pressure of CO_2 is an important processing parameter. The phases present in each recorded diffractogram during *in situ* HT-XRD as a function of temperature and CO_2 partial pressure are summarized in Figure 6 (all measured XRD patterns are shown in Figure S9).
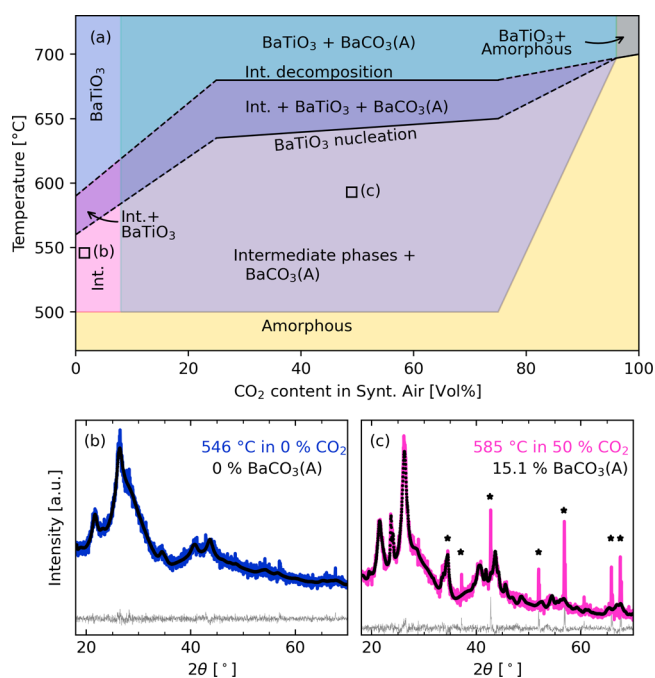
Figure 6. (a) Summary of the phases present as a function of both temperature and CO_2 partial pressure during *in situ* HT-XRD measurements of $BaTiO_3$ precursor powders. 0, 25, 50, 75, and 100 vol % CO_2 were used in the experiments. Intermediate phases are marked "Int.", and stippled lines are extrapolated boundaries. XRD patterns and Rietveld refinements of (b) $BaTiO_3$ precursor powder heated *in situ* to 546 °C in synthetic air (0% CO_2) and (c) $BaTiO_3$ precursor powder heated *in situ* to 585 °C in 50 vol % CO_2. Sharp peaks from the alumina crucible are marked with asterisks.

The results for the 0% CO_2 (synthetic air) correspond well with previous *ex situ* powder XRD results[21] and *in situ* XRD of $BaTiO_3$ films from the same precursor solution.[22] The formation of the intermediate phases was unaffected by increasing CO_2 partial pressure as they formed above 505 °C in all the gas mixtures, except in pure CO_2. However, for the powders heated in a CO_2-rich atmosphere, $BaCO_3$ (A) formed as a thermodynamically stable phase alongside the intermediates. The temperatures used during the *in situ* powder

HT-XRD measurements were not sufficient to remove $BaCO_3$ (A), so once formed the aragonite remained, even after formation of $BaTiO_3$. However, due to stoichiometric concerns, there should also be Ti-rich phases present, but since these are amorphous, they do not appear in the XRD patterns. The diffractogram of the sample heated to 546 °C in synthetic air (Figure 6b) demonstrates the presence of only the intermediate phases ($BaCO_3$ (C) and $BaTi_4O_9$), while at 585 °C in 50% CO_2 (Figure 6c), the powder contains about 15 wt % $BaCO_3$ (A) in addition to the intermediate phases. The refined cell parameters and crystallite sizes from the Rietveld refinements are listed in Table S4, where the poor crystallinity in this temperature region resulted in small refined crystallite sizes for both $BaCO_3$ (C) and $BaTi_4O_9$.

The stability of intermediate phases over $BaTiO_3$ nucleation exhibited a strong CO_2 dependence even though the formation temperature for the intermediates was unaffected by the CO_2 partial pressure. In synthetic air, the intermediates decomposed below 600 °C, while in a CO_2-rich atmosphere, they were still present at 675 °C (Figure 6a), which likely is caused by a stabilization of the $BaCO_3$ (C) phase by CO_2. The increased carbonate stability also affected the $BaTiO_3$ nucleation temperature, which was below 565 °C in synthetic air, but increased to above 650 °C in the CO_2-rich atmosphere. There were no significant differences in the phase evolution of the samples heated in 25–75% CO_2.

3. DISCUSSION

3.1. Transformation Pathway: Decomposition and Pyrolysis. The basicity of BaO and high stability of $BaCO_3$ make carbonate formation almost inevitable during the thermal processing of the $BaTiO_3$ precursor powder from an aqueous synthesis route. However, the phase evolution of the powders studied in this work followed the "oxycarbonate forming route" commonly reported for Pechini and sol–gel-based synthesis, instead of the solid-state reaction route. Therefore, it is probable that a mixed metal citric acid complex similar to those reported in refs 12, 14 formed in the precursor solution. A proposed transformation pathway is illustrated in Figure 7, and the decomposition and pyrolysis reactions can be divided into the following steps:
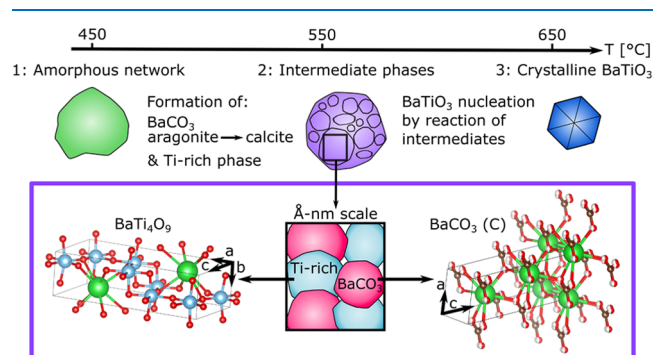
Figure 7. Illustration of the transformation pathway for $BaTiO_3$ precursor powders from an aqueous solution, from an amorphous network (step 1) at low temperatures to crystallization of $BaTiO_3$ (step 3) through reaction of the intermediate phases (step 2). The intermediate phases consist locally of small domains of $BaCO_3$ with a calcite structure and a Ti-rich phase with a $BaTi_4O_9$ structure, although there is limited long-range order for both phases. Structures made by VESTA.[40]

3.1.1. Decomposition (200–560 °C). At the start of this period, the nitrate decomposes, ammonia evaporates, and the decomposition/combustion of the organics initiates (step 1 in Figure 7). However, the wide RCOO⁻ stretching bands are still present, as seen from the *in situ* IR spectra of the powder precursors (Figure 1), originating from a variety of organic groups in the sample. The symmetric and asymmetric stretching bands of the RCOO⁻ groups become narrower and shift toward the asymmetric carbonate band as temperature is increased, demonstrating the preference for carbonate formation in this system. The organic removal (pyrolysis) can be expressed through the following proposed reaction (adapted from Ischenko *et al.*[19])

$$\text{organic network} \rightarrow BaCO_3\text{-like} + BaTi_4O_9 \qquad (2)$$

which occurs at the initiation of this temperature region, leaving only $BaCO_3$-like and $BaTi_4O_9$ phases in the system, with no long-range order. This is in accordance with the thermal analysis of the precursor powder, where a decrease in the mass fraction over a narrow temperature range is reported at 550 °C[21] corresponding to removal of the remaining organic compounds.

3.1.2. Carbonate Formation (480–570 °C). In this temperature range, the IR spectra only showed bands corresponding to carbonate (Figures 1 and 2), which were initially broad features of an amorphous carbonate species with a frequency corresponding to $BaCO_3$ (A) but quickly shifted toward the calcite frequency as the temperature was increased, according to the following proposed reaction

$$BaCO_3\text{-like (A)} \rightarrow BaCO_3(C) \qquad (3)$$
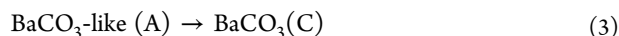
The carbonate frequency shift is accompanied by formation of a Ti-carbonate-like phase as indicated in the IR spectra (Figures 1 and 2), and weak reflections corresponding to the intermediate $BaCO_3$ (C) and $BaTi_4O_9$ phases are observed in the XRD patterns (Figure 3). The refined structures of $BaCO_3$ (C) and $BaTi_4O_9$ are displayed in Figure 7. Both the Rietveld and PDF refinements demonstrate that the crystallite size of each of the intermediate phases is in the nanorange or that the crystallinity is poor. This is further supported by the TEM images and SADP (Figure 5), showing limited crystallinity of the particles and small crystallites.

3.1.3. BaTiO₃ Nucleation and Growth (550–650 °C). Nucleation of $BaTiO_3$ occurs both directly from the amorphous phase during decomposition and through reaction of the intermediate phases according to the following proposed reaction (adapted from Ischenko *et al.*[19])

$$0.75BaCO_3(C) + 0.25BaTi_4O_9 \rightarrow BaTiO_3 + 0.75CO_2 \qquad (4)$$
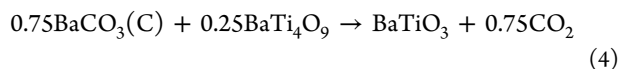
The nucleation of $BaTiO_3$ occurs homogeneously throughout the powder as TEM showed that the carbonate and Ti-rich phases are intimately mixed, and the metastable nature of the intermediate phases ensures complete decomposition.

3.2. Structures of the Intermediate Phases. The intermediate phases were found to consist locally of poorly crystalline and nanosized $BaCO_3$ (C) and $BaTi_4O_9$ with limited long-range order. Since $BaCO_3$ (A) is the thermodynamically stable structure in the temperature range of carbonate formation (eq 3),[38] the formation of $BaCO_3$ (C) is likely enabled due to one or several stabilizing mechanisms. The presence of titanium was observed to be a requirement for the calcite carbonate formation (Figure S4) and bands in the
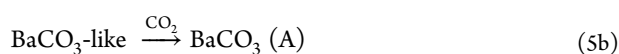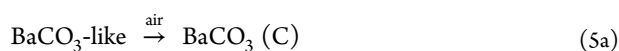
IR-spectra assigned to a Ti-carbonate-like group (Figures 1 and 2) formed alongside $BaCO_3$ (C) bands. Both observations demonstrate an interaction between the carbonate and Ti-rich intermediate phases, possibly at the interface between small domains of each phase as illustrated in Figure 7. The proposed model is further supported by the Rietveld and PDF refinements, which showed that the intermediate phases could be described by nanosized poorly crystalline $BaCO_3$ (C) and $BaTi_4O_9$ with limited long-range order. TEM further demonstrated limited crystallinity and small crystallites, but diffraction from both $BaCO_3$ (C) and $BaTi_4O_9$ was observed from individual (Figure 5c,e, respectively) and mixed particles (Figure 5f).

A similar model for the intermediate phases with $BaCO_3$ (C) stabilized by topotaxial templating on oxygen-deficient Ti−O interface layers was suggested by Ischenko *et al.*[20] Although the composition of the Ti-rich phase determined in this work, $BaTi_4O_9$, fits with the reported range given by Ischenko *et al.*,[19,20] the structure of $BaTi_4O_9$ does not seem to comply with the suggested $BaTiO_3$-like building blocks for the topotaxial templating model.[20] Moreover, the refined $BaCO_3$ (C) in this work has a compressed unit cell compared to the structure reported in the literature,[19,20,38] with 0.4 % expansion of the *a*-parameter but 6.9 % compression of the *c*-parameter. This reduction in unit cell volume is due to only slight vibrations of the carbonate groups instead of full rotations. O^{2-}-substitution, as suggested by Ischenko *et al.*[19,20] to act as a second stabilizing mechanism for $BaCO_3$ (C), was not investigated, but it seems likely given the deviating structure that the degree of substitution is different in this work compared to previous studies. However, since the intermediate phases are intimately mixed nanosized domains, with a certain degree of interaction between them (Figure 7), the structure could still follow the topotaxial templating model, even if the precursor chemistry and crystal structure of the intermediate phases deviate slightly. Stabilization of the calcite modification of $BaCO_3$ has been reported in mixed alkaline earth carbonates[41] or by quenching.[42] Intermediate carbonates with the calcite structure are also reported in $YBa_2Cu_3O_{7-x}$,[43] $Ba_{1-x}SrTiO_3$,[11] and $Ba_{1-x}Ca_xZr_yTi_{1-y}O_3$[23] systems. Controlling the carbonate formation was reported to be crucial for phase purity in $Ba_{0.85}Ca_{.15}Zr_{0.1}Ti_{0.9}O_3$ thin films.[23] Barium carbonate and Ti-rich intermediate phases are therefore probable intermediates during wet chemical processing of $BaTiO_3$-based materials, although the exact nature of these would depend on the precursor chemistry.

3.3. Influence of the Heating Rate and CO₂ on the Transformation Pathway for BaTiO₃. Slower heating generally decreased the temperature regions for the reaction occurring during the thermal decomposition of the $BaTiO_3$ precursor (Section 4.1), for certain heating rates. For fast heating (>1 °C/s), the transformation pathway is altered, and the intermediate phases are inhibited due to kinetics, giving direct $BaTiO_3$ nucleation from the amorphous network. This is in line with previous results on $BaTiO_3$ thin films from a similar precursor solution during fast heating (>1 °C/s).[22] Moreover, the *in situ* IR spectra of the precursor powders (Figure S3) show that carbonate formation was less pronounced for the slow heating (0.05 °C/s), which could relate to the metastable nature of the intermediate phases and the decomposition kinetics.

Increased partial pressure of CO_2 in the atmosphere stabilizes the intermediate phases over $BaTiO_3$ nucleation

(Figure 6) by drastically limiting the decomposition reaction in eq 4. For high CO_2 partial pressures (>25 vol % CO_2), the perovskite nucleation temperature increased more than 100 °C compared to that in synthetic air (0 vol % CO_2). Moreover, the temperature region for the coexistence of intermediates and perovskite increased for high CO_2 partial pressures, which means that even if the decomposition reaction in eq 4 can take place the high partial pressure of CO_2 serves as a kinetic limitation. A second effect of a high CO_2 partial pressure (>25 vol % CO_2) is the formation of the thermodynamically stable $BaCO_3$ (A), which once formed require temperatures above 700 °C to decompose. No secondary Ti-rich phases were observed by XRD alongside the perovskite once aragonite-type $BaCO_3$ formed; hence, titanium remains as unreacted amorphous $BaTi_4O_9$. $BaCO_3$ (A) formed at the same temperature as the intermediate phases; therefore, CO_2 stabilizes a second reaction during the organic removal step described by this modified version of eq 3

$$BaCO_3\text{-like} \xrightarrow{\text{air}} BaCO_3 \text{ (C)} \tag{5a}$$

$$BaCO_3\text{-like} \xrightarrow{CO_2} BaCO_3 \text{ (A)} \tag{5b}$$

leading to the formation of $BaCO_3$ (A) alongside the $BaCO_3$ (C) phase. The formation of a broad aragonite band in the IR spectra (Figure 2a−c) before the shift toward calcite formation when the precursor powders were annealed in air (eq 5a) might be caused by locally enhanced CO_2 partial pressure from decomposing organics. However, as the organics are further decomposed/combusted during heating, the enhanced CO_2 partial pressure decrease before the aragonite-type $BaCO_3$ can fully crystallize resulting in formation of $BaCO_3$ (C). It is also likely that the apparent stability of the intermediate phases observed in the total scattering data (Figure 3) is due to locally enhanced CO_2 partial pressure inside the capillaries during the experiments, which causes these phases to remain even during the prolonged annealing at 740 °C. Enhanced CO_2 levels would shift the reactions along the x-axis in Figure 6a, which also fits with the increased reaction temperatures observed. Although it is important to note that direct comparison between the different experiments carried out in this work cannot be done due to different reaction volumes used for the different techniques. The volume used for annealing will affect the kinetics of the reactions, which is why thin films[22] were observed to crystallize at a lower temperature than powders.[21] However, the trends for the decomposition of the precursor and crystallization can still be discussed, independent of reaction volume.

Carbonate formation is a well-known prevailing synthesis challenge in $BaTiO_3$-based materials and for Ba oxides, especially during wet chemical processing if the dissolved and atmospheric CO_2 levels are not controlled. The structure of the carbonate forming depends on the precursor chemistry, where the $BaCO_3$ (C) type is highly sensitive toward the processing conditions. However, the $BaCO_3$ (C) type could be preferable over the formation of $BaCO_3$ (A) due to the metastable nature of $BaCO_3$ (C), which under the right processing conditions results in phase-pure $BaTiO_3$ in the temperature range of 550−600 °C, as reported in this work.

4. CONCLUSIONS

The decomposition, pyrolysis, and crystallization reactions during synthesis of $BaTiO_3$ by an aqueous-based synthesis route were characterized by *in situ* IR and synchrotron X-ray total scattering. The *in situ* analysis revealed the transformation pathway for $BaTiO_3$ crystallization and the structure and composition of the intermediate metastable calcite-type $BaCO_3$ and $BaTi_4O_9$ phases that formed prior to $BaTiO_3$ nucleation. The crystallinity of the nanosized intermediate phases is poor as there is limited long-range order. $BaTiO_3$ nucleates both directly from an amorphous network but also through the diffusion-controlled reaction of the intermediate phases. Intimate mixing of the intermediate phases and their metastable nature ensure full decomposition in controlled atmospheres. However, the stability of the intermediates over $BaTiO_3$ formation is governed by the CO_2 partial pressure, where enhanced CO_2 levels stabilize calcite-type $BaCO_3$ but also leads to the formation of the thermodynamically stable aragonite-type $BaCO_3$. Therefore, control of the processing atmosphere is crucial when fabricating phase-pure $BaTiO_3$ through this aqueous synthesis route. Carbonate intermediate phases by similar formation mechanisms can also be expected for $BaTiO_3$-based materials and basic oxides in general.

5. EXPERIMENTAL SECTION

5.1. Synthesis. The preparation of the aqueous precursor solution has been reported previously.[21,22] Separate Ba- and Ti-complex solutions were prepared and then mixed in stochiometric ratios to make a final $BaTiO_3$ precursor solution with a concentration of 0.26 M. The Ba-solution was prepared by dissolving both EDTA (98%, Sigma-Aldrich, St. Louis, MO, USA) and citric acid (99.9%, Sigma-Aldrich, St. Louis, MO, USA) in deionized water to act as complexing agents for dissolved $Ba(NO_3)_2$ (99.9%, Sigma-Aldrich, St. Louis, MO, USA), while the Ti-solution was prepared by dissolving citric acid in deionized water followed by addition of Ti isopropoxide (97%, Sigma-Aldrich, St. Louis, MO, USA). Ammonia solution (30%, Sigma-Aldrich, St. Louis, MO, USA) was used to adjust the pH of the solutions to neutral prior to mixing.

$BaTiO_3$ precursor powder was prepared by drying the precursor solution at 150 °C for 24 h in air, resulting in a sponge-like brown material, which was crushed in an agar mortar to yield the precursor power. The $BaTiO_3$ precursor samples for *in situ* IR measurements were prepared by dispersing the precursor powder in deionized water and depositing droplets directly onto platinized silicon substrates (Pt/Si, SINTEF, Oslo, Norway). The droplets were flattened by draining most of the liquid of the substrate edge, leaving a wet precursor powder layer, which were dried at ambient temperature for 30−60 min. Precursor powders for *ex situ* X-ray total scattering and electron microscopy investigation of the intermediate phases were annealed at 530 °C for 1 h with a heating/cooling rate of 0.056 °C/s in air. The IR spectra of the prepared powders are included in Figure S1.

5.2. Characterization. Fourier-transform infrared spectra (FTIR, Vertex 80v, Bruker, Billerica, MA, USA) were recorded with a Praying Mantis Diffuse Reflection Accessory (Harrick Scientific Products Inc., Pleasantville, NY, USA) combined with the Praying Mantis High Temperature Reaction Chamber (Harrick Scientific Products Inc., Pleasantville, NY, USA). A flow of synthetic air was supplied through the reaction chamber during heating, except for one experiment, which was carried out without the dome of the reaction chamber in an ambient atmosphere and without instrument vacuum. A clean Pt/Si substrate was used as background and measured at

ambient temperature under the same conditions as the samples. The spectra were recorded in reflectance mode in the range of 400−4000 cm^{-1}, with a resolution of 4 cm^{-1}. Each scan took ~32 s, and the number of scans averaged depended on the heating rate; for 0.05 °C/s, 80 scans were averaged; for 0.2 °C/s, 40 scans were averaged; and for 0.5 and 1 °C/s, 20 scans were averaged. The IR spectra of the samples after heating were measured at ambient temperature in vacuum and without the dome of the reaction chamber, labeled "RT after".

In situ high-temperature X-ray diffraction (HT-XRD) on the precursor powder under a controlled CO_2 atmosphere was performed on a D8 Advance Diffractometer (Bruker, Billerica, MA, USA) with Cu Kα radiation (λ = 1.54 Å) equipped with a Vantec-1 SuperSpeed detector. The samples were prepared in a radiant heater sample holder of alumina. The partial pressure of CO_2 in synthetic air was varied in the range of 0−100%. The sample chamber was closed and purged with the desired gas mixture for 1 h before measurements were started. The diffractograms were recorded with a step size of 0.033° and 0.5 s scan time per step during a hold step at selected temperatures, and the heating rate in between hold steps was 0.2 °C/s. Rietveld refinements of the powder XRD patterns were done with the TOPAS software (v5, Bruker, Billerica, MA, USA).

X-ray total scattering data for pair distribution function (PDF) analysis of the $BaTiO_3$ precursor powders was collected on BL08W[44] at SPring-8 (Japan) using a flat 2D panel detector and a wavelength of 0.10765 Å. The time resolution of the recorded data was 5 s. For the *ex situ* measurement, a powder preannealed at 530 °C in air was filled in a Kapton tube (OD 1.05 mm, Goodfellow, England), and for the *in situ* measurements, the precursor powders were loaded in quartz capillaries (OD 1.5 mm, CharlesSupper Company, West-borough, USA) with glass wool on each side. The capillaries had continuous air flow of 0.12 L/min and were measured in transmission. A hot air blower was used to heat the samples continuously (0.17−1 °C/s) and then held at the maximum annealing temperature for 30−70 min. The 2D images were masked and integrated with the pyFAI python package,[45] where 5 patterns were averaged. Empty capillaries were used for background subtractions, which was done with the pdfgetx3 (v2.0.0) software using periodic structures.[46] The Q-range for the samples was 16−22 Å^{-1}, and the PDFs were refined with PDFGui (v1.1.2).[47]

For the transmission electron microscopy (TEM) investigation, a powder preannealed at 530 °C in air was dispersed in isopropanol in an ultrasound bath before depositing the powder particles on a holey carbon Cu-grid. TEM was performed on a JEOL JEM 2100 equipped with a LaB$_6$ electron gun. Selected area diffraction patterns (SADPs) were obtained using a circular aperture covering an area in real space with a diameter of approximately 750 nm.

ASSOCIATED CONTENT

Supporting Information

The Supporting Information is available free of charge at https://pubs.acs.org/doi/10.1021/acsomega.1c00089.

> Additional infrared spectra, *in situ* total scattering data, all XRD patterns, and refined values from PDF and Rietveld refinements are listed (PDF)

AUTHOR INFORMATION

Corresponding Author

Mari-Ann Einarsrud − *Department of Materials Science and Engineering, NTNU Norwegian University of Science and Technology, Trondheim 7491, Norway;* ● orcid.org/0000-0002-3017-1156; Email: mari-ann.einarsrud@ntnu.no

Authors

Kristine Bakken − *Department of Materials Science and Engineering, NTNU Norwegian University of Science and Technology, Trondheim 7491, Norway*

Viviann H. Pedersen − *Department of Materials Science and Engineering, NTNU Norwegian University of Science and Technology, Trondheim 7491, Norway*

Anders B. Blichfeld − *Department of Materials Science and Engineering, NTNU Norwegian University of Science and Technology, Trondheim 7491, Norway;* ● orcid.org/0000-0001-5631-4197

Inger-Emma Nylund − *Department of Materials Science and Engineering, NTNU Norwegian University of Science and Technology, Trondheim 7491, Norway*

Satoshi Tominaka − *International Center for Materials Nanoarchitectonics, National Institute for Materials Science, Ibaraki 305-0044, Japan;* ● orcid.org/0000-0001-6474-8665

Koji Ohara − *Diffraction and Scattering Division, Center for Synchrotron Radiation Research, Japan Synchrotron Radiation Research Institute, Hyogo 679-5198, Japan;* ● orcid.org/0000-0002-3134-512X

Tor Grande − *Department of Materials Science and Engineering, NTNU Norwegian University of Science and Technology, Trondheim 7491, Norway;* ● orcid.org/0000-0002-2709-1219

Complete contact information is available at:
https://pubs.acs.org/10.1021/acsomega.1c00089

Author Contributions

All authors have given approval to the final version of the manuscript.

Notes

The authors declare no competing financial interest.

ACKNOWLEDGMENTS

ABBREVIATIONS

as, asymmetric stretching; $BaCO_3$ (A), aragonite-type $BaCO_3$; $BaCO_3$ (C), calcite-type $BaCO_3$; BF, bright-field; BT, $BaTiO_3$; CSD, chemical solution deposition; HT-XRD, high temperature X-ray diffraction; Int, intermediate; IR, infrared spectroscopy; oop, out-of-plane; PDF, pair distribution function; SADP, selected area diffraction pattern; ss, symmetric stretching; TEM, transmission electron microscopy; XRD, X-ray diffraction.

REFERENCES

(1) Acosta, M.; Novak, N.; Rojas, V.; Patel, S.; Vaish, R.; Koruza, J.; Rossetti, G. A., Jr.; Rödel, J. $BaTiO_3$-based piezoelectrics: Fundamentals, current status, and perspectives. *Appl. Phys. Rev.* **2017**, *4*, No. 041305.

(2) Barin, I.; Platzki, G. *Thermochemical data of pure substances*. 3rd ed.; VCH: Weinheim, 1995; Vol. *1*.

(3) Aylward, G. H.; Findlay, T. J. V. *Si chemical data*. 6th ed.; Wiley: Milton, 2008.

(4) Sunde, T. O. L.; Grande, T.; Einarsrud, M.-A. Modified Pechini Synthesis of Oxide Powders and Thin Films. In *Handbook of Sol-Gel Science and Technology*, Klein, L.; Aparicio, M.; Jitianu, A. Eds. Springer International Publishing: Cham, 2016; pp. 1−30, DOI: 10.1007/978-3-319-19454-7_130-1.

(5) Schwartz, R. W.; Schneller, T.; Waser, R. Chemical solution deposition of electronic oxide films. *C. R. Chim.* **2004**, *7*, 433−461.

(6) Hasenkox, U.; Hoffmann, S.; Waser, R. Influence of precursor chemistry on the formation of $MTiO_3$ (M = Ba, Sr) ceramic thin films. *J. Sol-Gel Sci. Technol.* **1998**, *12*, 67−79.

(7) Ashiri, R.; Nemati, A.; Sasani Ghamsari, M.; Dastgahi, M. M. Nanothickness films, nanostructured films, and nanocrystals of barium titanate obtained directly by a newly developed sol-gel synthesis pathway. *J. Mater. Sci.: Mater. Electron.* **2014**, *25*, 5345−5355.

(8) Ashiri, R. On the solid-state formation of $BaTiO_3$ nanocrystals from mechanically activated $BaCO_3$ and TiO_2 powders: innovative mechanochemical processing, the mechanism involved, and phase and nanostructure evolutions. *RSC Adv.* **2016**, *6*, 17138−17150.

(9) Lotnyk, A.; Senz, S.; Hesse, D. Formation of $BaTiO_3$ thin films from (110) TiO_2 rutile single crystals and $BaCO_3$ by solid state reactions. *Solid State Ionics* **2006**, *177*, 429−436.

(10) Hoffmann, S.; Waser, R. Control of the morphology of CSD-prepared (Ba,Sr)TiO_3 thin films. *J. Eur. Ceram. Soc.* **1999**, *19*, 1339−1343.

(11) Chen, S.-Y.; Wang, H.-W.; Huang, L.-C. Role of an intermediate phase (Ba,Sr)$_2Ti_2O_5CO_3$ in doped (Ba$_{0.7}$Sr$_{0.3}$)TiO_3 thin films. *Mater. Chem. Phys.* **2003**, *77*, 632−638.

(12) Arima, M.; Kakihana, M.; Nakamura, Y.; Yashima, M.; Yoshimura, M. Polymerized complex route to barium titanate powders using barium-titanium mixed-metal citric acid complex. *J. Am. Ceram. Soc.* **1996**, *79*, 2847−2856.

(13) Fang, T.-T.; Wu, M.-S.; Tsai, J.-D. ^{13}C NMR study of the solution chemistry of barium titanium citrate gels prepared using the Pechini process. *J. Am. Ceram. Soc.* **2002**, *85*, 2984−2988.

(14) Kakihana, M.; Arima, M.; Nakamura, Y.; Yashima, M.; Yoshimura, M. Spectroscopic characterization of precursors used in the Pechini-type polymerizable complex processing of barium titanate. *Chem. Mater.* **1999**, *11*, 438−450.

(15) Tsay, J.-D.; Fang, T.-T.; Gubiotti, T. A.; Ying, J. Y. Evolution of the formation of barium titanate in the citrate process: the effect of the pH and the molar ratio of barium ion and citric acid. *J. Mater. Sci.* **1998**, *33*, 3721−3727.

(16) Durán, P.; Capel, F.; Gutierrez, D.; Tartaj, J.; Bañares, M. A.; Moure, C. Metal citrate polymerized complex thermal decomposition leading to the synthesis of $BaTiO_3$: effects of the precursor structure on the $BaTiO_3$ formation mechanism. *J. Mater. Chem.* **2001**, *11*, 1828−1836.

(17) Durán, P.; Gutierrez, D.; Tartaj, J.; Bañares, M. A.; Moure, C. On the formation of an oxycarbonate intermediate phase in the synthesis of $BaTiO_3$ from (Ba,Ti)-polymeric organic precursors. *J. Eur. Ceram. Soc.* **2002**, *22*, 797−807.

(18) Gablenz, S.; Abicht, H.-P.; Pippel, E.; Lichtenberger, O.; Woltersdorf, J. New evidence for an oxycarbonate phase as an intermediate step in $BaTiO_3$ preparation. *J. Eur. Ceram. Soc.* **2000**, *20*, 1053−1060.

(19) Ischenko, V.; Pippel, E.; Köferstein, R.; Abicht, H.-P.; Woltersdorf, J. Barium titanate via thermal decomposition of Ba,Ti-precursor complexes: The nature of the intermediate phases. *Solid State Sci.* **2007**, *9*, 21−26.

(20) Ischenko, V.; Woltersdorf, J.; Pippel, E.; Köferstein, R.; Abicht, H.-P. Formation of metastable calcite-type barium carbonate during low-temperature decomposition of (Ba,Ti)-precursor complexes. *Solid State Sci.* **2007**, *9*, 303−309.

(21) Raeder, T. M.; Bakken, K.; Glaum, J.; Einarsrud, M. A.; Grande, T. Enhanced in-plane ferroelectricity in $BaTiO_3$ thin films fabricated by aqueous chemical solution deposition. *AIP Adv.* **2018**, *8*, 105228.

(22) Bakken, K.; Blichfeld, A. B.; Chernyshov, D.; Grande, T.; Glaum, J.; Einarsrud, M.-A. Mechanisms for texture in $BaTiO_3$ thin films from aqueous chemical solution deposition. *J. Sol-Gel Sci. Technol.* **2020**, *95*, 562−572.

(23) Khomyakova, E.; Wenner, S.; Bakken, K.; Schultheiß, J.; Grande, T.; Glaum, J.; Einarsrud, M.-A. On the formation mechanism of $Ba_{0.85}Ca_{0.15}Zr_{0.1}Ti_{0.9}O_3$ thin films by aqueous chemical solution deposition. *J. Eur. Ceram. Soc.* **2020**, *40*, 5376−5383.

(24) Halder, S.; Schneller, T.; Waser, R. Crystallization temperature limit of (Ba,Sr)TiO_3 thin films prepared by a non oxocarbonate phase forming CSD route. *J. Sol-Gel Sci. Technol.* **2005**, *33*, 299−306.

(25) Ye, J.-Y.; Jiang, Y.-X.; Sheng, T.; Sun, S.-G. In-situ FTIR spectroscopic studies of electrocatalytic reactions and processes. *Nano Energy* **2016**, *29*, 414−427.

(26) Harks, P. P. R. M. L.; Mulder, F. M.; Notten, P. H. L. In situ methods for Li-ion battery research: A review of recent developments. *J. Power Sources* **2015**, *288*, 92−105.

(27) Lin, H.-J.; Li, H.-W.; Shao, H.; Lu, Y.; Asano, K. In situ measurement technologies on solid-state hydrogen storage materials: a review. *Mater. Today Energy* **2020**, *17*, 100463.

(28) Norby, P. In-situ XRD as a tool to understanding zeolite crystallization. *Curr. Opin. Colloid Interface Sci.* **2006**, *11*, 118−125.

(29) Jensen, K. M. Ø.; Tyrsted, C.; Bremholm, M.; Iversen, B. B. In Situ Studies of Solvothermal Synthesis of Energy Materials. *ChemSusChem* **2014**, *7*, 1594−1611.

(30) Nittala, K.; Mhin, S.; Jones, J. L.; Robinson, D. S.; Ihlefeld, J. F.; Brennecka, G. L. In situ x-ray diffraction of solution-derived ferroelectric thin films for quantitative phase and texture evolution measurement. *J. Appl. Phys.* **2012**, *112*, 104109.

(31) Cheetham, A. K.; Mellot, C. F. In Situ Studies of the Sol−Gel Synthesis of Materials. *Chem. Mater.* **1997**, *9*, 2269−2279.

(32) Bein, B.; Hsing, H.-C.; Callori, S. J.; Sinsheimer, J.; Chinta, P. V.; Headrick, R. L.; Dawber, M. In situ X-ray diffraction and the evolution of polarization during the growth of ferroelectric super-lattices. *Nat. Commun.* **2015**, *6*, 10136.

(33) Sinsheimer, J.; Callori, S. J.; Ziegler, B.; Bein, B.; Chinta, P. V.; Ashrafi, A.; Headrick, R. L.; Dawber, M. In-situ x-ray diffraction study of the growth of highly strained epitaxial $BaTiO_3$ thin films. *Appl. Phys. Lett.* **2013**, *103*, 242904.

(34) Nakamoto, K. *Infrared and Raman spectra of inorganic and coordination compounds : Pt. B : Applications in coordination, organometallic, and bioinorganic chemistry*. 5th ed.; Wiley: New York, 1997.

(35) Stuart, B. *Infrared Spectroscopy : Fundamentals and Applications*. Wiley: Chichester, 2004.

(36) Kwei, G. H.; Lawson, A. C.; Billinge, S. J. L.; Cheong, S. W. Structures of the ferroelectric phases of barium titanate. *J. Phys. Chem.* **1993**, *97*, 2368−2377.

(37) Kwei, G. H.; Billinge, S. J.; Cheong, S. W.; Saxton, J. G. Pair-distribution functions of ferroelectric perovskites: Direct observation of structural ground states. *Ferroelectrics* **1995**, *164*, 57−73.

(38) Antao, S. M.; Hassan, I. $BaCO_3$: high-temperature crystal structures and the Pmcn→R3m phase transition at 811°C. *Phys. Chem. Miner.* **2007**, *34*, 573−580.

(39) Morris, M. C., Mcmurdie, H. F., Evans, E. H., Paretzkin, B., Parker, H. S., Pyrros, N. P.; Hubbard, C. R. *Standard X-ray diffraction powder patterns*. National Bureau of Standards: US, 1984.

(40) Momma, K.; Izumi, F. VESTA 3 for three-dimensional visualization of crystal, volumetric and morphology data. *J. Appl. Crystallogr.* **2011**, *44*, 1272−1276.

(41) Lander, J. J. Polymorphism and Anion Rotational Disorder in the Alkaline Earth Carbonates. *J. Chem. Phys.* **1949**, *17*, 892−901.

(42) Strobel, R.; Maciejewski, M.; Pratsinis, S. E.; Baiker, A. Unprecedented formation of metastable monoclinic $BaCO_3$ nano-particles. *Thermochim. Acta* **2006**, *445*, 23−26.

(43) Rasi, S.; Soler, L.; Jareño, J.; Banchewski, J.; Guzman, R.; Mocuta, C.; Kreuzer, M.; Ricart, S.; Roura-Grabulosa, P.; Farjas, J.; Obradors, X.; Puig, T. Relevance of the Formation of Intermediate Non-Equilibrium Phases in $YBa_2Cu_3O_{7−x}$ Film Growth by Transient Liquid-Assisted Growth. *J. Phys. Chem. C* **2020**, *124*, 15574−15584.

(44) Ohara, K.; Tominaka, S.; Yamada, H.; Takahashi, M.; Yamaguchi, H.; Utsuno, F.; Umeki, T.; Yao, A.; Nakada, K.; Takemoto, M.; Hiroi, S.; Tsuji, N.; Wakihara, T. Time-resolved pair distribution function analysis of disordered materials on beamlines BL04B2 and BL08W at SPring-8. *J. Synchrotron Radiat.* **2018**, *25*, 1627−1633.

(45) Kieffer, J.; Valls, V.; Blanc, N.; Hennig, C. New tools for calibrating diffraction setups. *J. Synchrotron Rad.* **2020**, *27*, 558−566.

(46) Juhás, P.; Davis, T.; Farrow, C. L.; Billinge, S. J. L. PDFgetX3: a rapid and highly automatable program for processing powder diffraction data into total scattering pair distribution functions. *J. Appl. Crystallogr.* **2013**, *46*, 560−566.

(47) Farrow, C. L.; Juhas, P.; Liu, J. W.; Bryndin, D.; Božin, E. S.; Bloch, J.; Proffen, T.; Billinge, S. J. L. PDFfit2 and PDFgui: computer programs for studying nanostructure in crystals. *J. Phys.: Condens. Matter* **2007**, *19*, 335219.